#### **RESEARCH PAPER**



# Cyclic and post-cyclic axial behaviors of steel pipelines buried in dense sand

Chang Guo<sup>1</sup> · Chao Zhou<sup>2</sup> · Mohamed A. Meguid<sup>3</sup>

Received: 24 January 2025 / Accepted: 27 September 2025 © The Author(s) 2025

#### **Abstract**

The current design guidelines for underground pipelines do not consider cyclic axial soil-pipe interaction and its impact on post-cyclic pullout resistance, potentially leading to unsafe designs. This study conducted 12 large-scale physical model tests on steel pipes in dense sand to investigate their axial behavior during and after cyclic loading. A film-like sensor was employed to monitor soil-pipe interface contact pressure and earth pressure. The test program included different levels of pipe roughness, overburden pressure, and cyclic displacement. Given a cyclic displacement, the axial resistance in the first loading exceeds the guideline prediction, attributed to the increased interface contact pressures by constrained dilation. Subsequently, the axial resistance degrades over cycles. It stabilizes at a value that is roughness-dependent and smaller than the prediction because of the translation of the initial negative soil arching to positive soil arching on the pipe. The post-cyclic pullout resistance is smaller than the monotonic resistance without cycling when the cyclic displacement is relatively large (above 5 mm in this study). In contrast, the post-cyclic pullout resistance is above the monotonic resistance when the cyclic displacement is smaller due to cyclic loading-induced soil densification. The difference between post-cyclic and monotonic resistances for the rougher pipe is more significant.

Keywords Buried structures · Model tests · Pipes & pipelines · Soil/structure interaction · Repeated loading

| Abbreviations $D$ $d_{50}$ $H_{\rm c},H_{\rm c0},H_{\rm 0}$  | Pipe outer diameter Median particle size Buried depth of the pipe center, real buried depth of the pipe center in the experiment, and the buried depth from the ground sur- face to the sensor | $K_0$ $N$ $P$ $R_{\max}, R_a$              | Coefficient of lateral earth pressure at rest Cycle number Air pressure inside the flexible pneumatic bag Maximum height and average height devia- tions on the surface profile over a travel |  |  |  |
|--|--|--|---|--|--|--|
|  | race to the sensor   | $R_{ m n}$                                 | length of $d_{50}$<br>Normalized surface roughness<br>Axial resistance (maximum value of axial  |  |  |  |
| <ul><li></li></ul>   |  |  | force per unit length during axial loading to failure)  |  |  |  |
| Chang Guo<br>chang.guo@connect.polyu.hk  |  | $T_1$                                      | Mobilized axial resistance during the first loading at a cyclic amplitude of 20 mm, also  |  |  |  |
| Mohamed A. Meguid mohamed.meguid@mcgill.ca   |  |  | equal to axial resistance during monotonic loading without cyclic loading   |  |  |  |
| Department of Civil and Environmental Engineering, The Hong Kong Polytechnic University, Hung Hom, |  | $T_{ m u}$                                 | Ultimate value of axial resistance with a large number of cycles  |  |  |  |
|  | ng SAR, China  | $T_{\rm u}/T_1$                            | Degradation factor of axial resistance over cycle   |  |  |  |
| Research Hong Kor  | nt of Civil and Environmental Engineering, Institute for Sustainable Urban Development, The ng Polytechnic University, Hung Hom, ng SAR, China   | $T_{\rm p}$ $T_{\rm p}/T_1$ $u, u_{\rm A}$ | Axial resistance during post-cyclic pullout<br>Change factor of axial resistance<br>Axial displacement and axial cyclic dis-  |  |  |  |
| Department Montreal,   | nt of Civil Engineering, McGill University,<br>Canada  | , <sub>A</sub>                             | placement amplitude   |  |  |  |

Published online: 15 October 2025



 $\begin{array}{ll} \gamma' & \text{Effective unit weight of the backfill sand} \\ \delta, \, \delta_{\text{peak}}, \, \delta_{\text{cr}} & \text{Soil-interface friction angle and peak, and} \\ \sigma_{\text{c}'} & \text{Nominal vertical pressure at the pipe center} \\ \sigma_{e'} & \text{Theoretical vertical earth pressure without} \\ \sigma_{\text{considering stress redistribution}} \\ \varphi' & \text{Sand internal friction angle} \\ \end{array}$ 

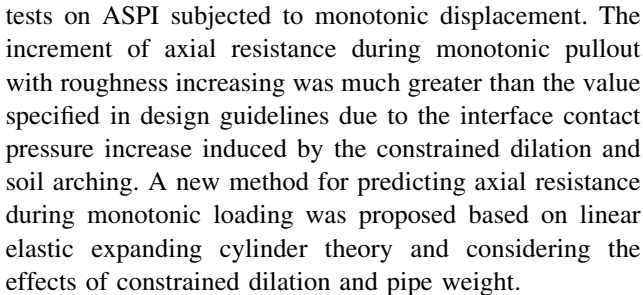
### 1 Introduction

Buried pipelines are routinely subjected to cyclic displacement relative to the surrounding soils during thermal expansion/contraction induced by periodic temperature variation of the ground or fluids (e.g., oil products or hot water) [1-3]. Moreover, a post-cyclic large axial relative displacement might happen due to the permanent ground displacement caused by geohazards and other activities [4–7]. Cyclic displacement significantly affects axial soil loads on pipes during and after the process [8–10]. A good understanding of these loads is essential because both underestimation and overestimation can cause unsafe pipeline design in certain cases. Underestimation results in a lower design value of pipeline strength, increasing the possibility of pipeline damage during its service life. In the event of overestimation, the actual constraint from the soil to the pipeline is smaller than the design value, leading to greater pipeline deformation and consequently increasing susceptibility to buckling failures (e.g., upheaval buckling and sharp bend ruptures) [11, 12].

Existing design guidelines [1, 11, 13] do not consider the effects of cyclic displacement. They calculate the axial resistance (maximum axial force per unit length during axial loading to failure) of pipes in the sand, *T*, as follows:

$$T = \pi D \frac{1 + K_0}{2} \gamma' H_c \tan \delta \tag{1}$$

where D is the pipe outer diameter;  $\gamma'$  is the effective unit weight of the backfill sand;  $H_c$  is the buried depth of the pipe center;  $\delta$  is the interface friction angle. This equation, based on the Mohr–Coulomb theory, assumes the average interface contact pressure on the pipe surface as a constant value of the mean of nominal vertical pressure at the pipe center,  $\sigma_c'$  (=  $\gamma'H_c$ ), and its lateral earth pressure at rest  $K_0\sigma_c'$ . The method's limitations in capturing the complex evolution of interface contact pressures in axial soil-pipe interaction (ASPI) of pipes subjected to monotonic displacement have been highlighted in previous studies [14–23]. For instance, Guo and Zhou [15] developed a new large-scale physical modeling system and conducted nine



Several studies on cyclic ASPI have also been carried out. Weidlich and Achmus [10] observed a reduction of axial resistance over cycles (degradation) in dense sand and an increase in loose sand through physical modeling tests with an HDPE-coated steel pipe, attributing interface contact pressure variation over cycles. Empirical relationships between the degradation factors and relative density and relative overburden height were proposed. Bilgin and Stewart [24] studied cyclic ASPI using an HDPE pipe under different temperatures in dense sands. The degradation was found to decrease with temperature growth because of variations in the radial diameter and hardness-dependent interface shear strength. Sheil, Martin et al. [22] conducted physical modeling using a heavy steel pipe coated with fusion-bonded epoxy. Alternating sets of larger amplitude (20 mm) and smaller amplitude (5 mm) cycles were applied. The potential effects of soil arching on pipe axial behavior were discussed. Although the above results are very useful, the understanding of cyclic ASPI seems limited. Firstly, surface roughness is a critical factor in cyclic and post-cyclic interface shear strength [8, 9, 25-30], but no study has explored its effects on cyclic ASPI. Secondly, the unique data of Sheil, Martin et al. [22] highlights the importance of cyclic amplitude on ASPI, but the use of alternating amplitudes cannot fully reveal its effects because soil-pipe interface behavior is path-dependent [8, 31]. Additionally, the mechanism of cyclic ASPI is still unclear due to limited data from the previous three studies. Finally, no studies have examined post-cyclic pullout behavior.

This study conducted twelve large-scale physical modeling tests to examine the cyclic and post-cyclic behaviors of ASPI, utilizing the experimental system and methodology developed by Guo and Zhou [15], which focused on the monotonic pullout behavior of pipelines. The primary objectives are (i) to investigate how surface roughness, burial pressure, and cyclic displacement amplitude influence axial resistance degradation over cycles, (ii) to examine the mechanisms underlying cyclic ASPI, and (iii) to explore the post-cyclic pullout behavior.

### 1.1 Experimental system and instrumentation

Figure 1 shows the experimental system for assessing ASPI in this study. Details on the system and



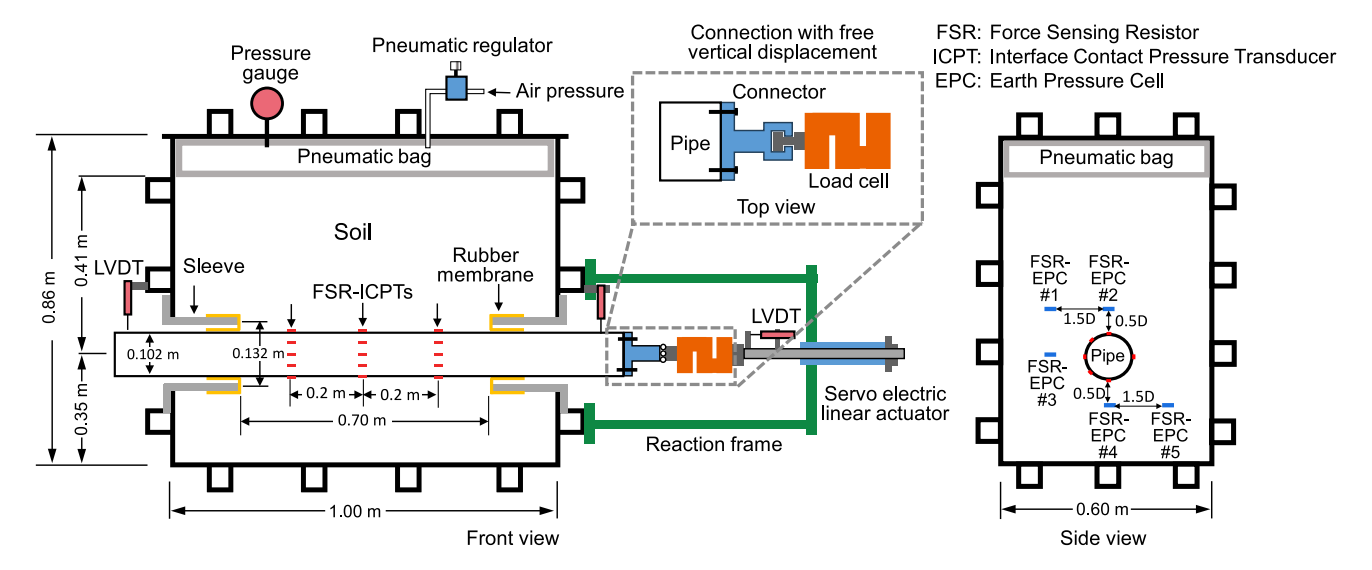


Fig. 1 Schematic diagram of the experimental system [15]

instrumentation can be found in Guo and Zhou [15]. It comprises a steel box to simulate the pipeline trench, pipes, an axial actuation subsystem, and a flexible pneumatic bag.

The internal dimensions of the steel box are  $1.0 \times 0.8 \times 0.6 \text{ m}^3$ . The axial actuation subsystem applies axial displacement to the pipe. A specially designed connector enables free vertical movement of the pipe. To simulate different buried depths of the pipe within the box, the flexible pneumatic bag, with dimensions matching the box interior, was positioned between the sample and the top cap. The air pressure, P, inside the bag is regulated to replicate the equivalent burial depth under field conditions. The nominal pressure at the center,  $\sigma_c$ , could follow the equation  $\sigma_c$  =  $\gamma'H_{c0}$  + P, where  $H_{c0}$  represents the actual burial depth from the ground surface to the pipe's center.

The presence of rigid front and rear walls in the box can lead to a nonuniform shear stress distribution along the pipe's axial direction [15, 17]. To minimize the boundary effects caused by these walls, two sleeves are installed inwardly at the openings of the front and rear walls. The pipe and sleeves are coaxially aligned, creating an 8.5 mm gap (equivalent to 22  $d_{50}$  of sand used in this study), which accommodates pipe settlement (less than 5 mm in this study) and a soil-pipe interface shear zone (ranging from 2 to 10  $d_{50}$  [32]). Two flexible rubber membranes with a nominal thickness of 1.5 mm connect the pipe to the inner ends of the sleeves. The sections of these membranes between the sleeves and the pipe prevent soil leakage through the gap and provide sufficient lateral support for the surrounding soil. Meanwhile, due to their flexibility, these membrane sections deform slightly in response to pipe movement and soil displacement, resulting in minimal friction between the pipe and the membrane. This configuration eliminates soil-pipe interaction near the front and rear walls and ensures a 0.7 m effective soil-pipe interaction section. Axial strain, measured using an optical fiber sensor based on the optical frequency domain reflectometry technique, is found to be distributed nearly linearly along the effective soil-pipe interaction section, confirming the uniformity of shear stress distribution and the effective minimization of boundary effects from the rigid walls. Further details regarding the minimization of boundary effects can be found in Guo and Zhou [15].

Two linear variable differential transformers (LVDTs) were utilized to measure the pipe's vertical displacement. A load cell with a capacity of  $\pm~10~kN$  and an LVDT with 50 mm were used to monitor the axial force and displacement.

A cutting-edge sensor, Force Sensing Resistor (FSR), was used to measure the earth and soil-pipe interface contact pressure [33]. This piezoresistive sensor's electrical conductance varies as a function of the applied pressure. Its thinness and flexibility are advantageous in mitigating the arching effects on sensors and adapting to curved surfaces [34, 35]. Five FSR-based earth pressure cells (FSR-EPCs) were attached to a steel slice with 1 mm in thickness and secured with epoxy adhesive to measure the vertical earth pressure at different depths as the distribution in Fig. 1. Eighteen FSR-based interface contact pressure transducers (FSR-ICPTs) were pasted on the pipe surface to assess soilpipe interface contact pressures over three cross sections spaced 0.2 m apart. Each cross section featured six FSR-ICPTs positioned at key points: the crown, one shoulder, two springlines, one haunch, and the invert. The performance of FSR-based sensors is highly dependent on their specific installation conditions. Therefore, post-installation calibration was conducted in sealed chambers. The air pressure within these chambers was controlled in a loop:



increasing from 0 to 200 kPa (loading path), then decreasing back to 0 kPa (unloading path). Calibration results from eighteen FSR-based sensors showed that along the loading and unloading paths, the hysteresis error for the loop was around 14.2%. To minimize the effects of nonlinearity and hysteresis on the test results, a nonlinear signal processing method was employed. The calibration data were fitted using the smoothing spline algorithm in MATLAB, and measured electrical conductance values were converted to pressure values based on this fit. The calibration curve obtained during loading was used to analyze the first loading (the loading of the first cycle) process of the physical model tests, as the loading histories on the sensors are similar in both scenarios. Subsequently, the loading and unloading calibration curves were averaged and used to analyze the physical model data from the first unloading (the unloading of the first cycle), as this simplified method provides a relatively accurate and practical approach to data analysis. Further details regarding FSRbased sensors can be found in Guo and Zhou [36].

## 2 Experimental materials

In practice, cohesionless and free-draining soils are typically recommended as backfilling and embedment materials [37]. Hence, standard medium sand from Fujian Province, China, with a particle size of  $0.25 \sim 0.5$  mm, was selected as the test soil. Its properties are summarized in Table 1. The target relative density was 85%, meeting the compaction requirement in practice [37].

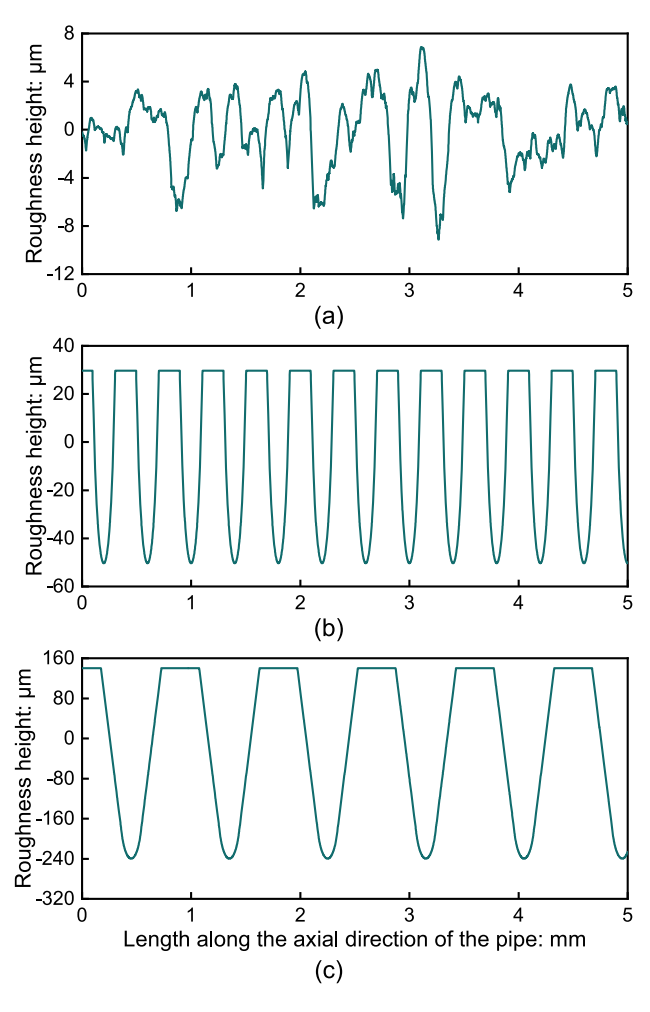
Hot-rolled seamless steel pipes with a nominal outer diameter of 102 mm and a thickness of 4 mm, commonly used as gas pipes and water mains in Hong Kong, were used [38, 39]. More pipe material parameters are provided in Guo and Zhou [15]. Three pipes with varying surface

Table 1 Sand properties

| Soil properties                                | Values          |  |
|--|-----------------|--|
| Specific gravity                               | 2.68            |  |
| Particle size: mm                              | $0.25 \sim 0.5$ |  |
| Median particle size, $d_{50}$ : mm            | 0.375           |  |
| Maximum void ratio                             | 0.797           |  |
| Minimum void ratio                             | 0.526           |  |
| Relative density: %                            | 85              |  |
| Dry unit weight, $\gamma'$ : kN/m <sup>3</sup> | 17.0            |  |
| Peak friction angle*: °                        | 39.6            |  |
| Critical state friction angle*: °              | 32.8            |  |

<sup>\*</sup>Measured by direct shear tests with effective normal stresses of 17, 34, 50, and 100 kPa

roughness (smooth, intermediate, and rough) were prepared. Surface roughness was quantified using the normalized roughness  $(R_n)$  proposed by Kishida and Uesugi [40]:  $R_n = R_{max}/d_{50}$ , where  $R_{max}$  is the maximum height deviation on the surface profile over a travel length of  $d_{50}$ . The classification method for rough, intermediate, and smooth interfaces is based on the variation of interface friction angles with  $R_n$ . Paikowsky, Player et al. [41] suggest critical  $R_n$  values of 0.02 and 0.5 to differentiate smooth-intermediate and intermediate-rough interfaces. The profiles of the pipe surface are illustrated in Fig. 2. The raw seamless steel pipe with  $R_n$  of 0.04, measured by SJ-210, Mitutoyo, is considered smooth. Rough and intermediate pipes were machined using a turning method to achieve ribbed profiles with  $R_n$  values of 1.01 and 0.21, respectively, along the pipe's axial direction. It is important to note that the current study does not consider the impact of temperature on variations in pipe diameter [3]. The linear temperature expansion coefficient of the pipe



**Fig. 2** Profiles of pipe surface: (a) smooth pipe (measured by SJ-210, Mitutoyo); (b) intermediate pipe (treated by turning method); (c) rough pipe (treated by turning method)



between 0 and 100 °C is  $17.3 \times 10^{-6}$  °C<sup>-1</sup>. For a temperature change of 30 °C, the potential temperature-induced variation in pipe diameter would be no more than 0.053 mm (equivalent to only 0.14  $d_{50}$ ). Therefore, the ignorance of the radial thermal expansion would only slightly underestimate the pullout resistance.

The sand internal friction angle and the sand-interface friction angles at the dry condition were measured by direct shear tests, as presented in Table 1 and Table 2. The shear rate is 0.02 mm/s, the axial speed of the pipe in subsequent physical modeling. Effective normal stresses were set at 17, 34, 50, and 100 kPa, aligning with values of  $\sigma_c$  in the physical models. Moreover, sand-interface direct shear tests were conducted under dry, partially saturated, and fully saturated conditions [4]. The results confirm that moisture content has a minimal impact on the shear behavior since the test sand is coarse and clean. Therefore, for simplicity, only dry sand was used in the physical model tests.

### 2.1 Testing program

Two series of cyclic tests were performed, as detailed in Table 3. Series I encompassed seven tests aimed at investigating the influence of surface roughness and overburden pressure on cyclic ASPI. Smooth and rough pipes were tested at  $\sigma_c$ ' of 17, 34, and 50 kPa, equivalent to burial depths of around 1, 2, and 3 m, respectively. These depths are common in practice, meeting the minimum buried depth of 0.8 m in practice [42]. The intermediate pipe underwent a test at a  $\sigma_c'$  of 34 kPa. Cyclic displacement amplitude  $(u_A)$  for this series was 20 mm, a common value where the axial force could basically reach its residual value in previous studies [15, 22, 23]. The number of cycles, N, for smooth, intermediate, and rough pipes was 5, 10, and 10, respectively. These values were determined based on the following physical model tests, where their maximum force per unit length during the N-th loading consistently stabilized.

Series II examined the impact of cycle displacement amplitude on cyclic ASPI at a  $\sigma_{\rm c}'$  of 34 kPa. A critical displacement of approximately 5 mm, where the axial

force of rough pipes peaked during the first loading, was observed in tests of Series I. Consequently,  $u_A$  for Series II was set to 2.5, 5, and 10 mm to assess cyclic ASPI under conditions where  $u_A$  is less than, equal to, and greater than the critical displacement, respectively. Post-cyclic behavior was also explored in Series II. After 20 cycles, the maximum force per unit length during the N-th loading at the given cyclic displacement consistently stabilized in most of the following physical model tests. A post-cyclic pullout with an amplitude of 20 mm was then applied (see Fig. 3).

The axial displacement rate in these two series was set to 0.02 mm/s, a common value in previous studies [22, 43]. As shown in Fig. 3, each test was conducted under a oneway, displacement-controlled cyclic loading regime, consistent with Weidlich and Achmus [10] and Sheil, Martin et al. [22]. The cycling is displacement-controlled rather than load-controlled. This method more closely reflects field conditions, as the potential axial thermal deformation of the pipe remains constant under a given temperature variation. However, it should be noted that actual field conditions are more complex, as the resistance provided by the surrounding soil can constrain axial deformation. Based on findings from subsequent physical model tests, in which axial resistance typically degrades over cycles, the cyclic displacement amplitude under field conditions would be expected to increase with each cycle and stabilize once the axial resistance reaches a steady state.

#### 2.2 Sample preparation and testing procedures

The sand pluviation method was used to prepare dry, dense, and uniform samples, emulating the dumping technique in engineering practice. The model was prepared in 25 mm layers. After preparing the sample and placing the pneumatic bag and top cap, the air pressure was adjusted to simulate overburden pressure. This condition was maintained for about 30 min until sensor readings, such as vertical displacement and earth pressure, stabilized. Finally, axial displacement was applied.

Table 2 Pipe surface conditions and soil-pipe interface properties

| Pipe type    | R <sub>max</sub> : mm | $R_{\mathrm{n}}^{}*}$ | R <sub>a</sub> : mm | Peak interface friction angle, $\delta_{\rm peak}^{\dagger}$ : ° | Critical state interface friction angle, $\delta_{\rm cr}^{\dagger}$ : ° |
|--------------|-----------------------|-----------------------|---------------------|--|--|
| Smooth       | 0.015                 | 0.04                  | 0.0024              | 18.4   | 17.3   |
| Intermediate | 0.08                  | 0.21                  | 0.1789              | 34.7   | 29.4   |
| Rough        | 0.38                  | 1.01                  | 0.2098              | 37.9   | 33.5   |

<sup>\*</sup> $R_{\rm n}$  Normalized surface roughness using  $R_{\rm max}/d_{50}$ 



<sup>&</sup>lt;sup>†</sup>Measured by direct interface shear tests with effective normal stresses of 17, 34, 50, and 100 kPa

Table 3 Testing program

| Test series                                | Reference     | Pipe type    | Nominal pressure on the center, $\sigma_c$ ': kPa | Cyclic displacement amplitude, $u_A$ : mm | Cycle number, <i>N</i> | Post-cyclic pullout |
|--|---------------|--------------|---|---|------------------------|---------------------|
| Series I                                   | S-17-A20      | Smooth       | 17  | 20  | 5                      | No                  |
| roughness and pressure effects on          | S-34-A20      | Smooth       | 34  | 20  | 5                      | No                  |
| cyclic ASPI                                | S-50-A20      | Smooth       | 50  | 20  | 5                      | No                  |
|  | R-17-A20      | Rough        | 17  | 20  | 10                     | No                  |
|  | R-34-A20      | Rough        | 34  | 20  | 10                     | No                  |
|  | R-50-A20      | Rough        | 50  | 20  | 10                     | No                  |
|  | M-34-<br>A20  | Intermediate | 34  | 20  | 10                     | No                  |
| Series II amplitude effects on cyclic ASPI | S-34-<br>A2.5 | Smooth       | 34  | 2.5                                       | 20                     | Yes                 |
| and post-cyclic pullout                    | S-34-A5       | Smooth       | 34  | 5   | 20                     | Yes                 |
|  | R-34-<br>A2.5 | Rough        | 34  | 2.5                                       | 20                     | Yes                 |
|  | R-34-A5       | Rough        | 34  | 5   | 20                     | Yes                 |
|  | R-34-A10      | Rough        | 34  | 10  | 20                     | Yes                 |

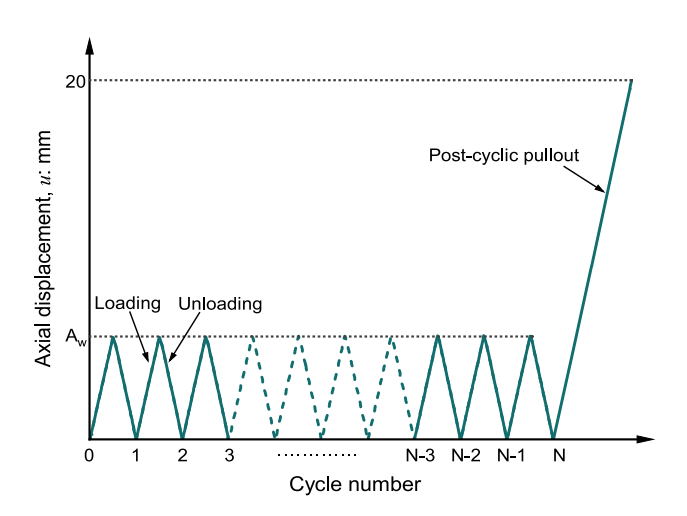


Fig. 3 Schematic diagram of cyclic and post-cyclic paths

# 3 Experimental results and discussion

# 3.1 Effects of roughness and nominal overburden pressure on cyclic ASPI

Figure 4 shows the relationship between axial displacement and the axial force in Series I. The figure includes axial resistances predicted by Eq. (1) using the measured interface peak friction angle ( $\delta_{peak}$ ) and the critical state friction angle ( $\delta_{cr}$ ) as  $\delta$  for comparison. As Guo and Zhou [15] discussed, the first loading curve for the rough pipe exhibits pronounced displacement-softening behavior,

whereas the curve for the smooth pipe demonstrates minimal softening. The predictions using Eq. (1) and  $\delta_{\rm peak}$  substantially underestimate axial resistance during the first loading  $(T_1)$  for both rough and smooth pipes, with discrepancies ranging from 64 to 95% and 35 to 60%, respectively. This underestimation is primarily attributed to the ignorance of the constrained dilation at the soil-pipe interface.

Upon the first unloading, both rough and smooth pipes exhibit displacement-hardening behavior, with the curve's shape being influenced by the surface roughness. These curve shapes are consistent with typical cyclic interface shear behavior [8, 44]. Both rough and smooth pipes experience a notable degradation in axial resistance compared to  $T_1$ , consistent with previous research on dense sand in soil-interface shearing tests and ASPI modeling [8, 9, 44, 45]. This degradation is mainly linked to the change of soil state (e.g., porosity and stress) around the pipe, as discussed later.

The second loading resembles the first unloading instead of the first loading. It indicates that the change of soil state has been largely finished in the first loading, which is supported by the stress path given later. The curve of the second unloading exhibits an approximate rotational symmetry with the second loading. Results of the following cycles remain qualitatively similar. The axial resistance decreases slightly over the cycles and eventually stabilizes to an ultimate value ( $T_{\rm u}$ ). This trend is consistent with the findings of Weidlich and Achmus [10] and Bilgin and Stewart [24]. It is reasonable to assume that the axial



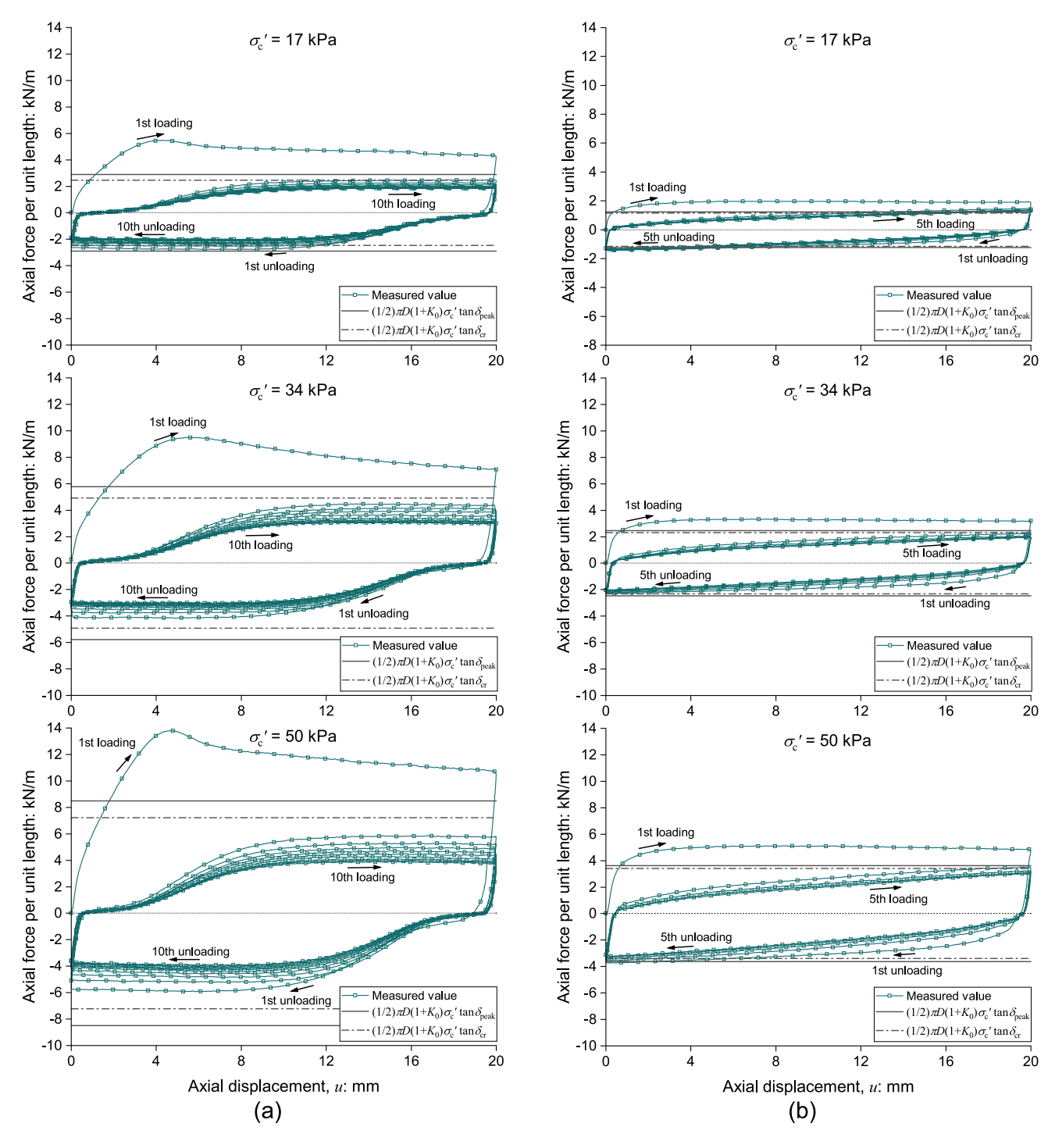


Fig. 4 Effects of nominal pressure at pipe center and surface roughness on cyclic axial force (Series I,  $u_A = 20$  mm): (a) rough pipe and (b) smooth pipe

resistance remains unchanged in subsequent cycles. For the smooth pipe, changes in axial resistances became consistently minimal by the fifth cycle, while for the rough and intermediate pipes, this occurred by the tenth cycle. Consequently, the tests were stopped at these points. The values of  $T_{\rm u}$  are generally lower than the predictions using

Eq. (1) and  $\delta_{\rm cr}$ , with the maximum discrepancy reaching 48%. This difference indicates a potential risk for pipeline systems after being subjected to thermal expansion and contraction cycles. The significant drop in soil resistance would increase the load transferred to other vulnerable pipeline components (e.g., valve stations and sharp bends)



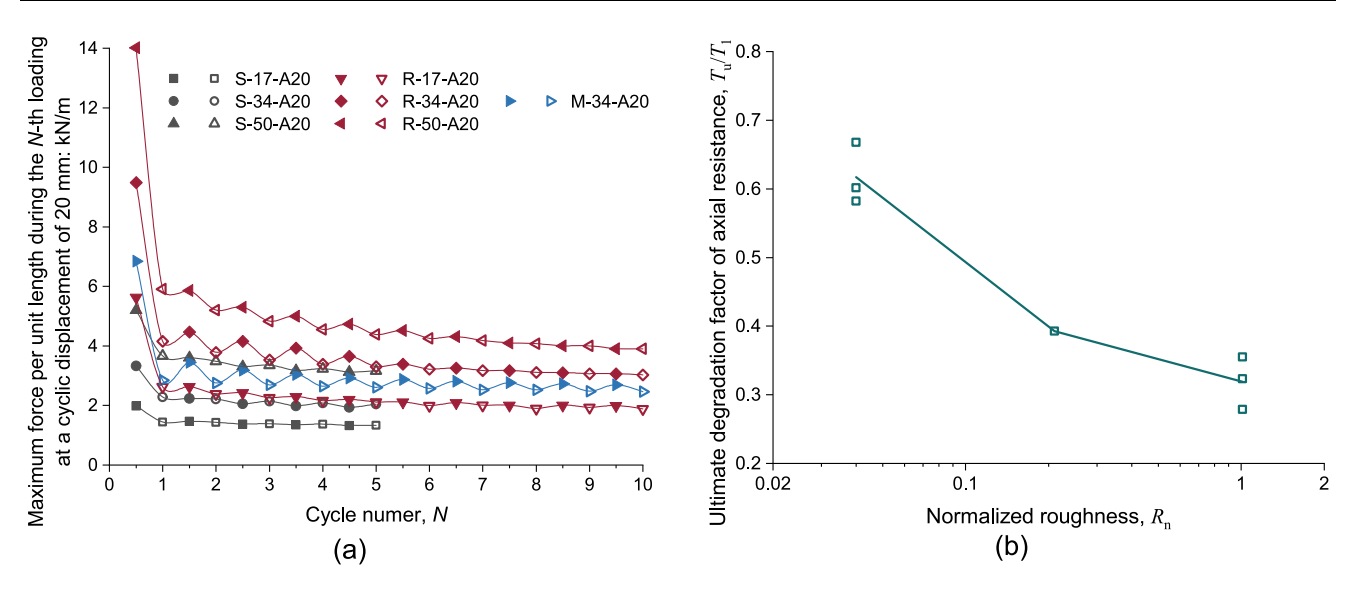


Fig. 5 Cyclic degradation of axial resistance: (a) axial resistance versus cycle number; (b) ultimate degradation factor versus surface roughness

rather than soils, increasing the risk of buckling failures [11].

Figure 5a illustrates the degradation of axial resistance over cycles for all tests in Series I. The axial resistance decreases with the cycles, especially during the first two cycles. The axial resistance during loading is generally slightly higher than that during the unloading of the preceding cycle, likely arising from the asymmetry in the testing setup. The influence of nominal pressure on the ultimate degradation factors,  $T_u/T_1$ , is small, with a reduction of less than 10% when  $\sigma_c$  increases from 17 to 50 kPa. However,  $T_{\rm u}/T_{\rm 1}$  decreases sharply with increasing roughness, as shown in Fig. 5b. The reduction results from more prominent constrained dilation and interface friction strength mobilization on rough pipes, as discussed later. The average values of  $T_u/T_1$  for rough, intermediate, and smooth pipes are about 0.62, 0.39, and 0.32, respectively.  $T_{\rm u}$  can be calculated using the predicted equation of  $T_1$ proposed by Guo and Zhou [15] and the above data on degradation factors. The obtained  $T_{\rm u}$  can be used by engineers as the lower bound of axial resistance (i.e., the resistance after many cycles) to calculate the potential maximum axial strain of the pipe upon thermal expansion and contraction.

# 3.2 Evolution of interface contact pressures during cyclic loading

Fig. 6 illustrates the typical evolution process of soil-pipe interface contact pressure measured by FSR-ICPTs using the results obtained from rough and smooth pipes under a surcharge of 34 kPa. The variation in interface contact pressures at corresponding positions across the three cross sections is generally within 10% of the average value. As a

result, the average values from the three cross sections are presented directly. During cyclic loading, the difference in interface contact pressure between the left and right springlines remains below 4 kPa, demonstrating good symmetry. Therefore, the interface contact pressures at the pipe's shoulders, springlines, and haunches are assumed to be mirrored between the left and right sides, and the average of the left and right springlines is reported as the springline result. Theoretical values of average interface contact pressure,  $(1 + K_0)\sigma_c^2/2$  (23.2 kPa, where  $K_0$  is taken as 1-sin  $\varphi'$ ), according to ALA [1], are also incorporated for comparison. As Guo and Zhou [15] mentioned, before testing, the average interface contact pressures for both pipes closely approximate their theoretical values. However, during the first loading, the average interface contact pressure of the rough pipe increases owing to constrained dilation [23, 46, 47], where the soil surrounding the pipe restricts the dilation of the soil-pipe interface, resulting in increased interface contact pressures. Furthermore, the tendency of dilation increases with increasing interface roughness (see Fig. 6).

During the first unloading, the average interface contact pressure decreases before increasing to a value slightly smaller than the theoretical value. The loading and unloading paths of the subsequent cycles exhibit consistent behavior with the first unloading. The variation in interface contact pressure of the rough pipe (reaching a minimum of 6.6 kPa) is more significant than that of the smooth pipe (minimum of 13.9 kPa). This behavior is related to the reconstruction of the interface shear band, which can be explained using the force chain evolution supported by discrete element method (DEM) simulations [26, 48, 49]. Before loading, the preferential orientation of contacts is typically perpendicular to pipes. Upon the first loading, the



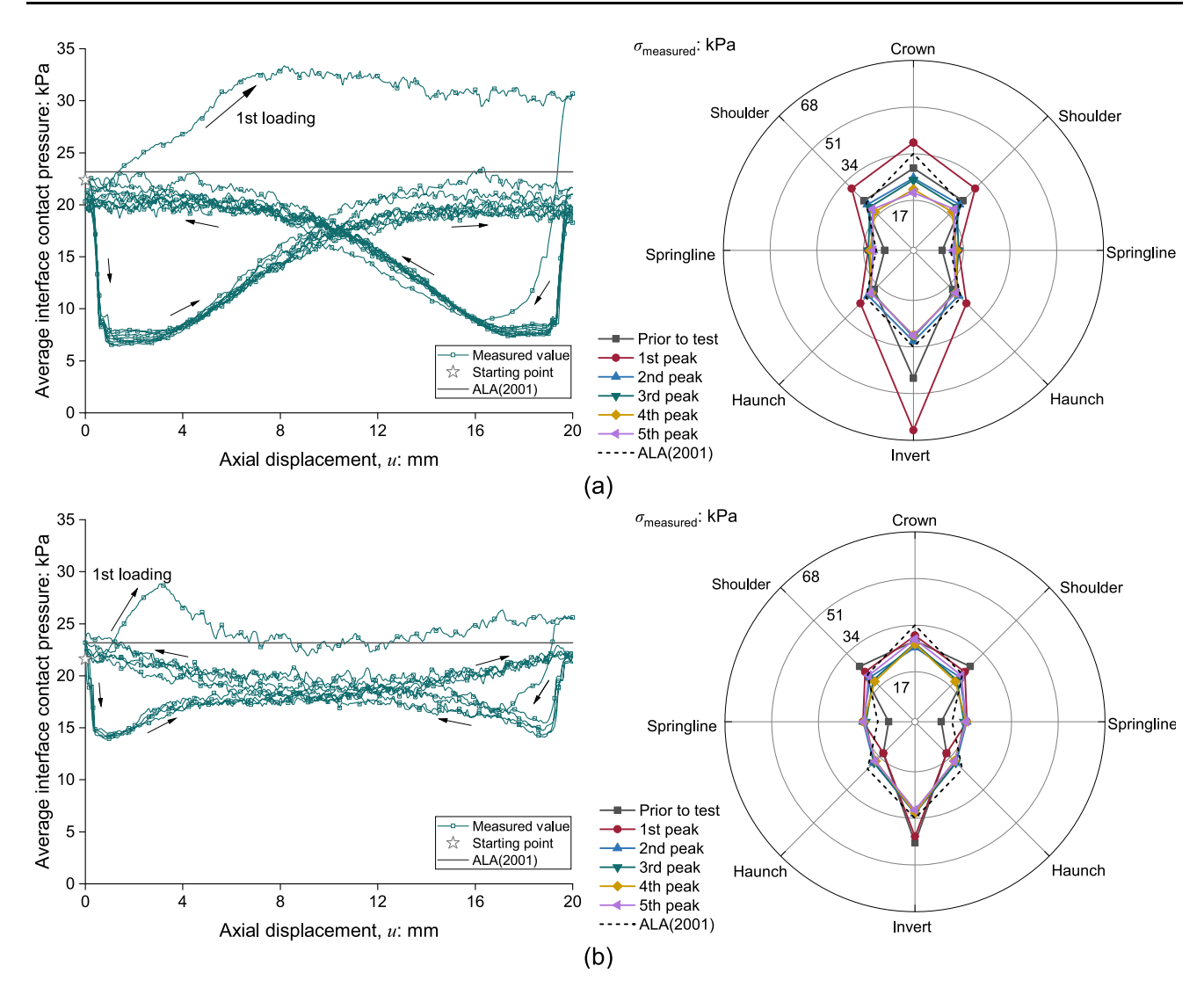


Fig. 6 Typical evolution of interface contact pressure ( $\sigma_c' = 34 \text{ kPa}$ ,  $u_A = 20 \text{ mm}$ ): (a) rough pipe and (b) smooth pipe

preferential orientation in the vicinity of the interface rotates, inclining toward the pipe's axial direction. This process forms a shear band with strong force chains due to the constrained dilation. During the subsequent loading reversal, the preferential orientation of contacts reverses with the loading direction, resulting in the vanishment and subsequent reconstruction of strong force chains, causing a decrease followed by an increase in soil-pipe interface contact pressures. The thicker interface shear band of rough pipes leads to a larger periodic change in average interface contact pressure compared to that of smooth pipes.

Figure 6 also illustrates the typical interface contact pressure distribution. According to ALA [1], the assumed interface contact pressure is  $\sigma_{\rm c}'$  (34 kPa) at the crown and invert,  $K_0\sigma_{\rm c}'$  (12.3 kPa) at the springlines, and  $(1+K_0)\sigma_{\rm c}'/2$  (23.2 kPa) at the shoulders and haunches, respectively. Before testing, the differences between measured and expected values typically do not exceed 25% of the

expected values. During cyclic loading and unloading, interface contact pressures are redistributed with varying trends across different pipes. For the rough pipe, all interface contact pressures notably increase during the first loading, particularly at the crown and invert, reaching 38 and 64 kPa, respectively. Subsequent cycles bring all interface contact pressures, except that of the crown, closer to the predicted value with a deviation of less than 8.5%. The pressure at the pipe crown is 26% lower than expected, explaining the slightly smaller axial resistances of the rough pipe than the prediction during the second loading phase in Fig. 4. In subsequent cycles, pressures at springlines, haunches, and the invert stabilize at theoretical values, while those at the crown and shoulders continue to decrease, reaching 19.9 and 19.8 kPa, respectively, by the fifth loading. This trend of interface contact pressure variation is consistent with the study of Weidlich and



Achmus [10] and corresponds to the decreasing axial resistance over cycles in Fig. 4.

As for the smooth pipe, the increase in interface contact pressure during the first loading primarily focuses on the springlines, reaching around 17.7 kPa, corresponding to the limited increase in average interface contact pressure. In the second loading, interface contact pressures at shoulders, haunches, and the invert align closely with predicted values, with a deviation not exceeding 5.8%. In subsequent cycles, pressures at haunches and the invert also maintain proximity to theoretical values, while those at the crown and shoulders continue to decrease, although the magnitude of the decrease is not as large as that observed in the rough pipe, with interface contact pressures reaching 28.8 and 22.6 kPa, respectively, by the fifth loading.

# 3.3 Pipe settlement behavior during cyclic loading

Figure 7 illustrates the typical results of the axial and vertical displacements of rough and smooth pipes under a surcharge of 34 kPa. Only the first five cycles of the rough pipe are shown to facilitate comparison with those of the smooth pipe. Both pipes settle continuously over cycles, aligning with the results of Sheil, Martin et al. [22]. These settlement curves reflect the influence of soil-pipe interface behavior on the soil beneath the pipe, encompassing two interrelated mechanisms. The first mechanism is associated with the shearing-induced contraction or dilation behavior within the soil-pipe interface shear zone. Contractive soil behavior in the shear zone below the pipe tends to promote pipe settlement, as the soil supporting the pipe becomes densified and the overall interface contact pressure between the soil and pipe decreases. In contrast, dilative soil behavior tends to cause pipe uplift and an increase in the interface contact pressure between the soil and pipe. The second mechanism relates to changes in the soil-pipe interface contact pressure, which are induced by the first mechanism. Variations in the interface contact pressure at the invert of the pipe lead to changes in the soil density beneath the pipe, thereby affecting the vertical movement of the pipe. Both the increase and cyclic variation of vertical effective stress in this region contribute to vertical compression, thereby promoting pipe settlement.

During the first loading (the first and second stages in Fig. 7) of the rough pipe, the vertical displacement is dominated by the soil compression due to vertical effective stress variation. The rapid settlement in the first stage corresponds to the increasing average interface contact pressure depicted in Fig. 6a and increasing axial force in Fig. 4a, while the unchanged vertical displacement in the second stage aligns with the stable interface contact pressure and axial force at the same displacement. The third and fourth stages of the rough pipe in Fig. 7 display an opposing pattern to the first two stages. The vertical position experienced a descent followed by an ascent, even if the average interface contact pressure decreased and then increased. This discrepancy arises from the interface shear contraction or dilation behavior of the lower portion of the interface shear band. During the typical interface shearing, the soil typically undergoes interface shear contraction followed by dilation [50]. Thus, the interface shear contraction/dilation behavior of the interface shear band tends to induce the settling and then rising of pipes. This trend is dominant and opposed to the average effective stress effects on pipe vertical displacement during the third and fourth stages in Fig. 7. At the fifth stage, the dilation might become minimal so that the average effective stress effects on pipe vertical displacement take back their dominance. The results of the smooth pipe and subsequent cycles of the

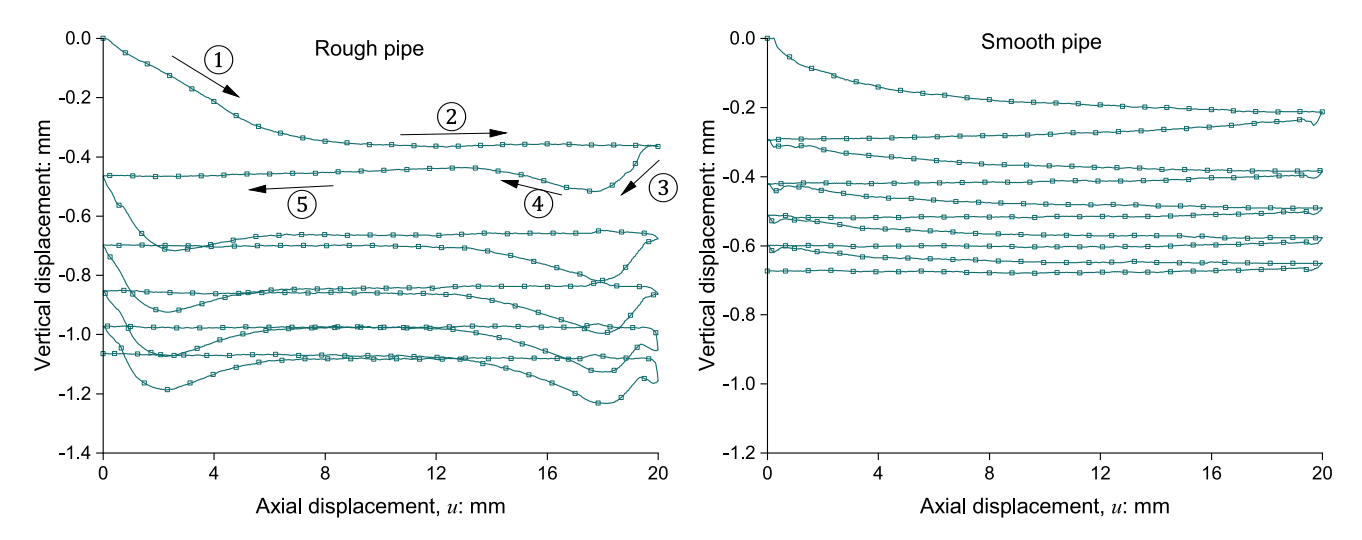


Fig. 7 Typical pipe settlement behavior ( $\sigma_c' = 34$  kPa,  $u_A = 20$  mm, first five cycles)



rough pipe exhibit similar settlement patterns to those observed in the first cycle of the rough pipe.

Figure 8 depicts irreversible settlement, defined as the change in the pipe's initial vertical position of each cycle relative to its vertical position before testing. Irreversible settlement increases with the cycle number and surface roughness. This is consistent with the periodic variation of average effective stress and prior research on cyclic interface shear behavior [8, 9, 25, 27]: the larger magnitude of average effective stress in tests of rough pipe leads to larger soil compression than that of smooth pipes; higher roughness causes a larger permanent volumetric decrease on the soil-pipe interface. The relationship between the settlement and  $\sigma_{\rm c}'$  within the range of 17  $\sim$  50 kPa is not monotonic. This may be attributed to the opposing effects of the two mechanisms described above. As  $\sigma_{c}'$  decreases, dilation increases. According to the first mechanism, greater dilation at the lower portion of the soil-pipe interface would tend to cause pipe uplift. In contrast, however, greater constrained dilation also leads to a larger increase in vertical effective stress, which, through the second mechanism, results in increased compression-induced settlement. These compensating effects may offset each other, leading to the non-monotonic trend.

### 3.4 Soil arching effects on cyclic ASPI

The evolution and redistribution of interface contact pressures shown in Fig. 6 can be linked to the development of soil arching on the pipe over cycles. The soil arching is normally categorized into negative and positive soil arching [22, 51–53]. Negative soil arching, also known as passive soil arching, typically occurs when the buried structure deforms or moves less than the surrounding soil. This relative displacement induces internal shear and stress

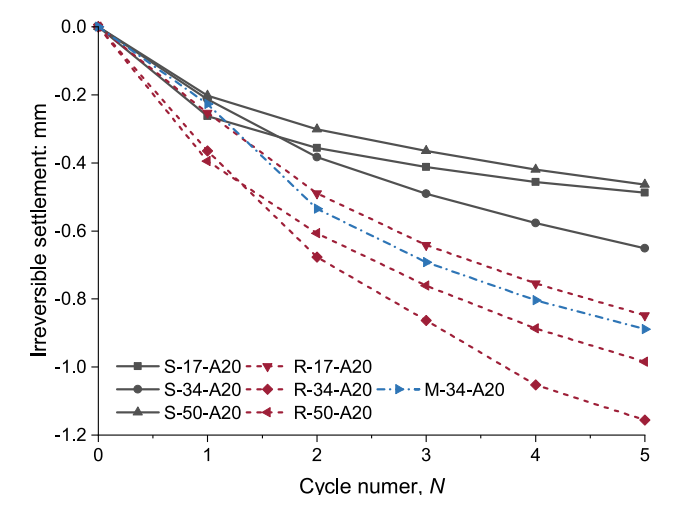


Fig. 8 Irreversible settlement versus cyclic number ( $u_A = 20 \text{ mm}$ )

redistribution, resulting in a greater load being transferred onto the structure. Conversely, positive soil arching, or active arching, arises when the structure deforms or moves more than the adjacent soil, thereby reducing the load imposed on the structure. During cyclic ASPI, the evolution of soil arching is simultaneously influenced by the combined effects of the soil-pipe interface dilation and pipe settlement behavior. This process is schematically represented in Fig. 9, where the "ultimate loading" in the figure denotes the loading when  $T_{\rm u}$  is reached. It is also supported by data on vertical earth pressure measured by FSR-EPCs in Fig. 10, where the theoretical vertical earth pressure,  $\sigma_{\rm e}'$ , calculated without considering stress redistribution  $(\sigma_e' = \gamma' H_0 + P)$ , where  $H_0$  represents the buried depth from the ground surface to the sensor), is included for comparison.

As discussed by Guo and Zhou [15] and Guo, Zhou et al. [17], before the tests, the pipe might undergo a slight negative soil arching, where the soil at the sides of the pipe is subjected to a downward movement relative to the soil above the pipe due to the stiffening effect. This relative movement forces more overburden pressure on shoulders and the invert of the pipe. Evidence for this is shown in Fig. 6, where the measured interface contact pressures at the pipe shoulder and invert are slightly larger than their theoretical values. Additional evidence is provided in Fig. 10, where the measured vertical earth pressures above and below the rough pipes (FSR-EPCs # 2 and #4) are slightly higher than their respective  $\sigma_{\rm e}'$ , while pressures at the pipe sides (FSR-EPCs #1, #3, and #5) are slightly lower than their respective  $\sigma_{\rm e}'$ .

During the first loading of rough pipes, the pronounced interface dilation emphasizes an additional negative soil arching due to further relative vertical displacement, significantly increasing the interface contact pressures at the crown and the invert (see Fig. 6). Correspondingly, these vertical earth pressures above and below the rough pipes (FSR-EPCs # 2 and #4) increase due to the additional negative arching effects and the pressure rise induced by the constrained dilation on the pipe, while pressures at the pipe sides (FSR-EPCs #1, #3, and #5) show a slight decrease during shearing. For smooth pipes, the more dominant mechanism is that the pipe movement disrupts the initial negative soil arching equilibrium, causing a notable increase in interface contact pressure at the springlines (see Fig. 6). The vertical earth pressure variation for smooth pipes in Fig. 10 is not as marked as that for rough pipes.

In the first unloading and subsequent cycles, the negative soil arching may be largely disrupted due to the reconstruction of the shear band and pipe settlement. The soil around the pipe interface in Series I tests also transitions from a dense to a critical state, which is demonstrated



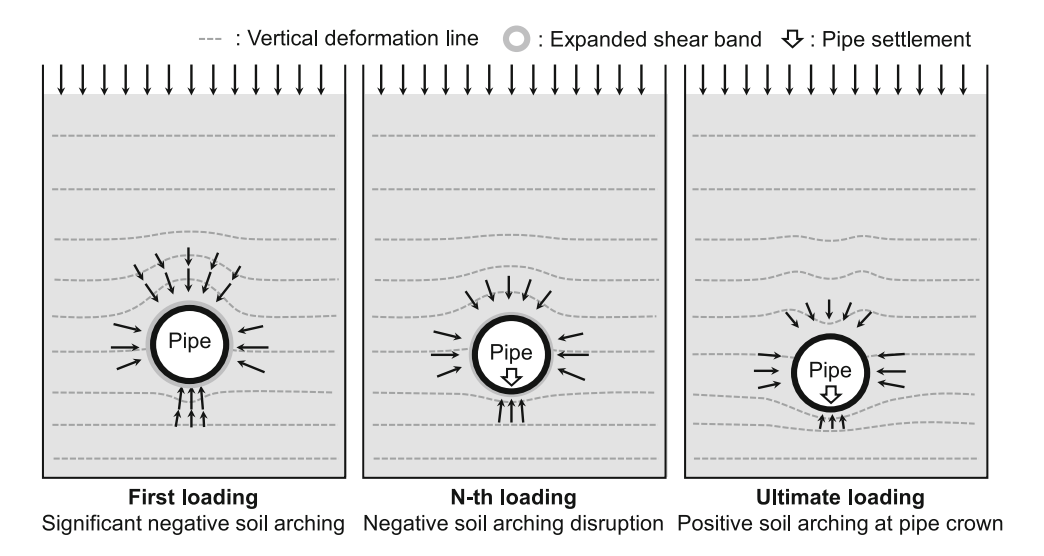


Fig. 9 Schematic diagram of soil arching evolution during cycling

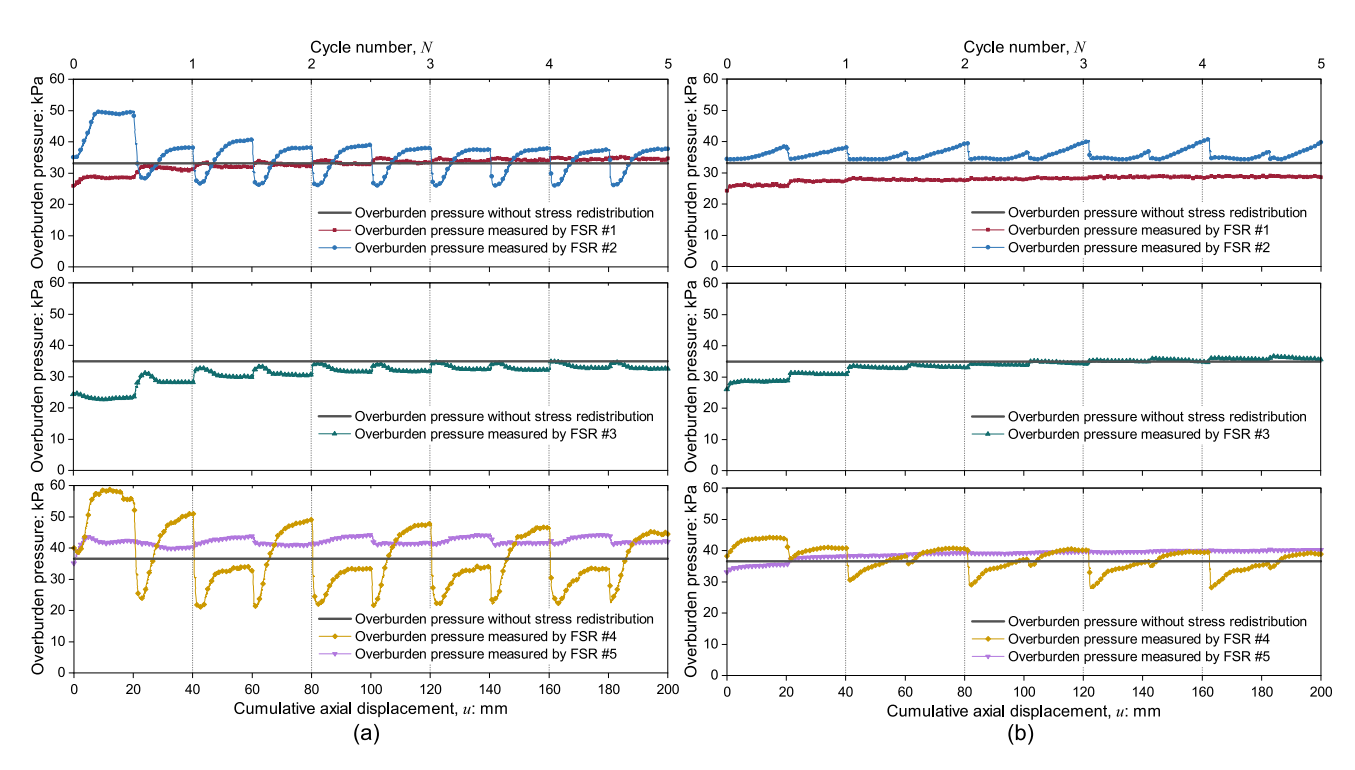


Fig. 10 Typical evolution of earth pressure ( $\sigma_c' = 34$  kPa,  $u_A = 20$  mm, first five cycles): (a) rough pipe and (b) smooth pipe

later. Consequently, the stress distribution closely aligns with the predicted condition for the second loading, with an axial resistance nearing the prediction based on  $\delta_{cr}$  (see Fig. 4).

Meanwhile, the ongoing settlement might lead to the pipe being subjected to a downward movement relative to the soil at the sides of the pipe (see Fig. 7 and Fig. 8). It may reverse the negative soil arching to a positive soil

arching on the upper part of the pipe. Evidence for this transition is provided by the observed decrease in interface contact pressure at the crown and shoulders over successive cycles (see Fig. 6). This decrease is more pronounced for rough pipes due to their higher settlement (see Fig. 8). The earth pressures in Fig. 10 further support the occurrence of this soil arching transition. First, although the vertical earth pressures above and below the rough pipes increase during



each loading and unloading path, they decrease during each reversal of the axial direction. This indicates that the disappearance of interface dilation during axial direction reversal eliminates the additional passive soil arching previously mentioned. Second, nearly all vertical earth pressures gradually approach their respective  $\sigma_{\rm e}'$  values over cycles, suggesting a weakening of negative soil arching. Third, some vertical earth pressures above and below the rough pipes eventually fall below their  $\sigma_{\rm e}'$ , demonstrating the emergence of positive soil arching.

# 3.5 Effects of cyclic displacement amplitude on ASPI

Fig. 11a shows the typical cyclic behavior of rough pipes in Series II with a 5 mm amplitude. The axial force-displacement curve during the first loading aligns with the early portion of the curve with 20 mm amplitude (see Fig. 4a), but 5 mm displacement is insufficient to induce softening. In the subsequent loading and unloading cycles, consistent with Fig. 4a, the maximum axial force degrades over cycles, but the degradation rate is not as pronounced as that observed with a 20 mm amplitude. Furthermore, the maximum axial force during unloading exhibits minimal variation over cycles and is typically lower than the corresponding maximum axial force in the loading path of the same cycle. The above behavior of axial force is related to the interface contact pressure evolution. During the first loading of rough pipe with 5 mm amplitude, same as Fig. 6a, the average interface contact pressure consistently increases due to the constrained dilation and stops at around 31 kPa. During the first unloading, the average interface contact pressure decreases to around 12.5 kPa, but there is no subsequent rise, being different from the trend in Fig. 6a, likely because the reconstruction of the shear band is not fully finished within the 5 mm displacement. Moreover, the reduction in interface contact pressure can well explain the lower maximum axial force during unloading than that during the previous loading from the same cycle. In the second and third loadings, the average interface contact pressure increases to around 26 and 23 kPa, higher than the theoretical values by ALA [1], aligning with the corresponding higher maximum axial force than predicted. In the subsequent cycles, the pressure increments during the loading path continuously decline.

Fig. 11b shows the results of smooth pipes subjected to cyclic loading with a 5 mm amplitude. The axial force and interface contact pressure evolutions of smooth pipes are similar to those under 20 mm amplitude in Fig. 4b, suggesting limited effects of amplitude on smooth pipes.

Fig. 11 also illustrates the pipe settlement behavior. The average effective stress variation caused by soil compression and interface shear contraction/dilation behavior of the

upper portion of the interface shear band is also reflected in the shapes of vertical displacement curves. The irreversible settlement over cycles under 5 mm amplitude is close to that under 20 mm in Fig. 7. It might be due to the limited amplitude effects on the average effective stress variation during cyclic shearing.

Fig. 12 presents the stress paths at the soil-pipe interfaces in physical modeling, offering insights into ASPI. The failure envelopes for three interfaces, determined through constant normal loading (CNL) interface direct shear tests, are included for reference. The first cycle's stress paths for rough pipes with 20 mm amplitude include six stages, resembling the typical stress path observed in constant normal stiffness (CNS) tests on rough interfaces [45, 54]. Initially, the stress path ascends vertically, indicating primarily elastic friction angle mobilization. It then shifts to the second stage by moving upwards to the right, reflecting an increase in average interface contact pressure due to constrained dilation. After reaching the peak failure envelope, the stress paths in the third stage go downwards to the right, approaching the critical state envelope. With the reversal of axial displacement direction, the fourth and fifth stages are marked by a significant reduction in axial force and average interface contact pressure, attributed to the vanishment of strong force chains in the shear band. It follows an increase in the sixth stage as these chains are reestablished. Subsequent cycles follow a path similar to the first unloading. They never surpass the critical state interface envelopes after the first unloading, indicating a mobilization from peak to critical interface shear strength. For rough pipes with amplitudes of 2.5, 5, and 10 mm, the shear strength mobilization to the critical state remains incomplete during the first loading, influencing subsequent axial pipe behavior. The stress paths for a 10 mm amplitude do not fully transition from peak to critical state in the third stage of its first loading, resulting in subsequent paths reaching the zone between the peak and critical state envelopes. For a 5 mm amplitude, the stress paths only approach the peak envelope by the end of the second stage in the first loading. Hence, in later cycles, they mobilize from approaching the peak envelopes to approaching the critical state envelopes. In the case of a 2.5 mm amplitude, the first loading stress paths do not reach the peak envelope, leading to a slower shear strength mobilization and, consequently, less degradation in the maximum axial force, as shown in Fig. 11. The soil-pipe interface mobilization mechanism for smooth pipes, as illustrated in Fig. 12b, is similar. The only notable distinction is that the first cycle stress path includes an additional stage (the third stage in Fig. 12b), where the path turns to the upper left due to a decrease in average interface contact pressure caused by soil arching disturbance. In addition, there are slight deviations between the interface stress paths and the



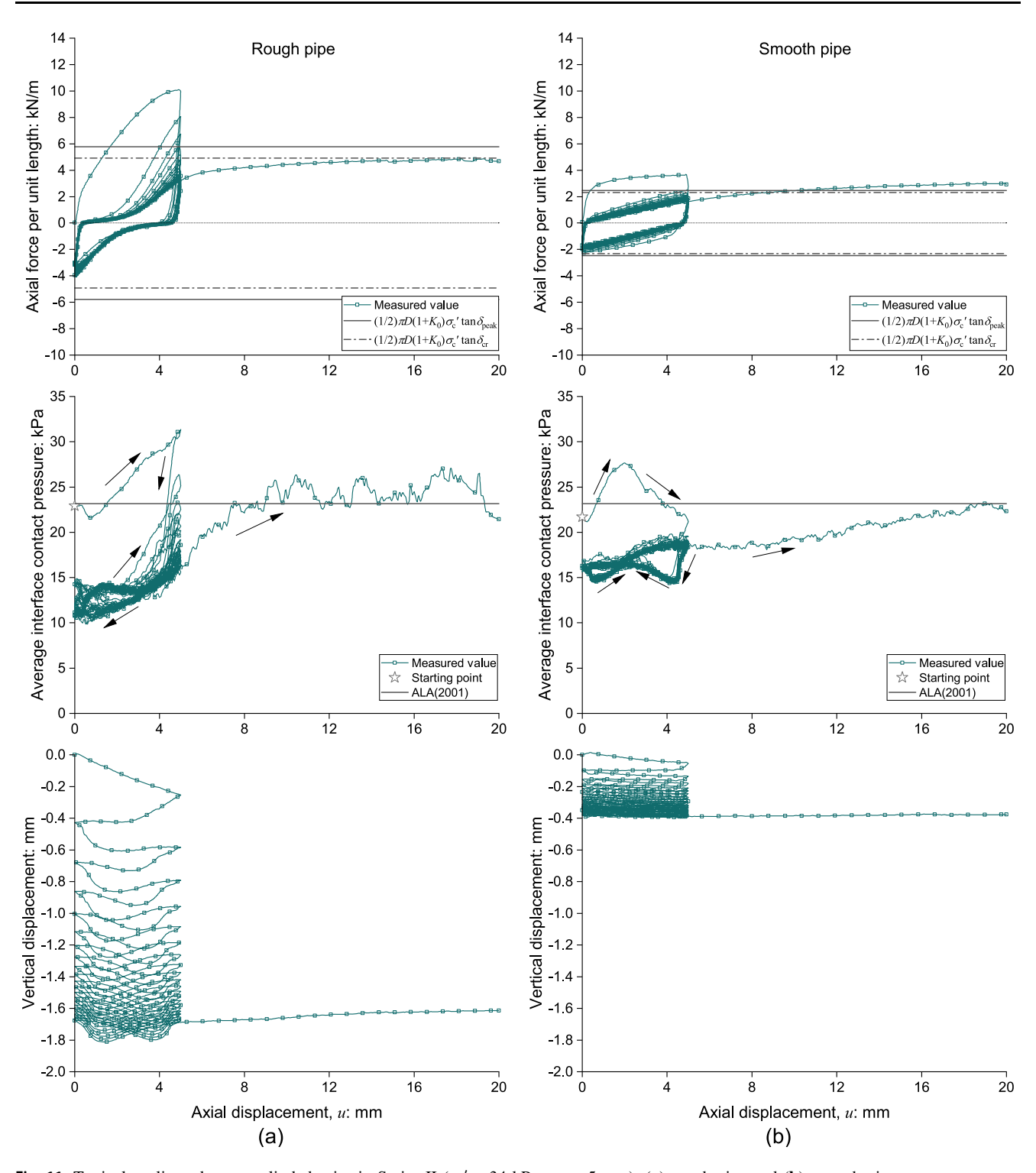


Fig. 11 Typical cyclic and post-cyclic behavior in Series II ( $\sigma_c' = 34$  kPa,  $u_A = 5$  mm): (a) rough pipe and (b) smooth pipe

interface failure envelopes. This may be attributed to two factors. First, the average interface contact pressure is calculated from discrete FSR-ICPT measurements. Second, the rigid boundary effects in the interface direct shear tests were not minimized to the same extent as in the physical model tests [55]. As a result, there may be minor

differences in the measured interface failure envelopes. Numerical simulations with ideal boundary conditions and comprehensive data, such as the DEM simulations conducted by Guo, Zhou et al. [17], can provide more accurate results.



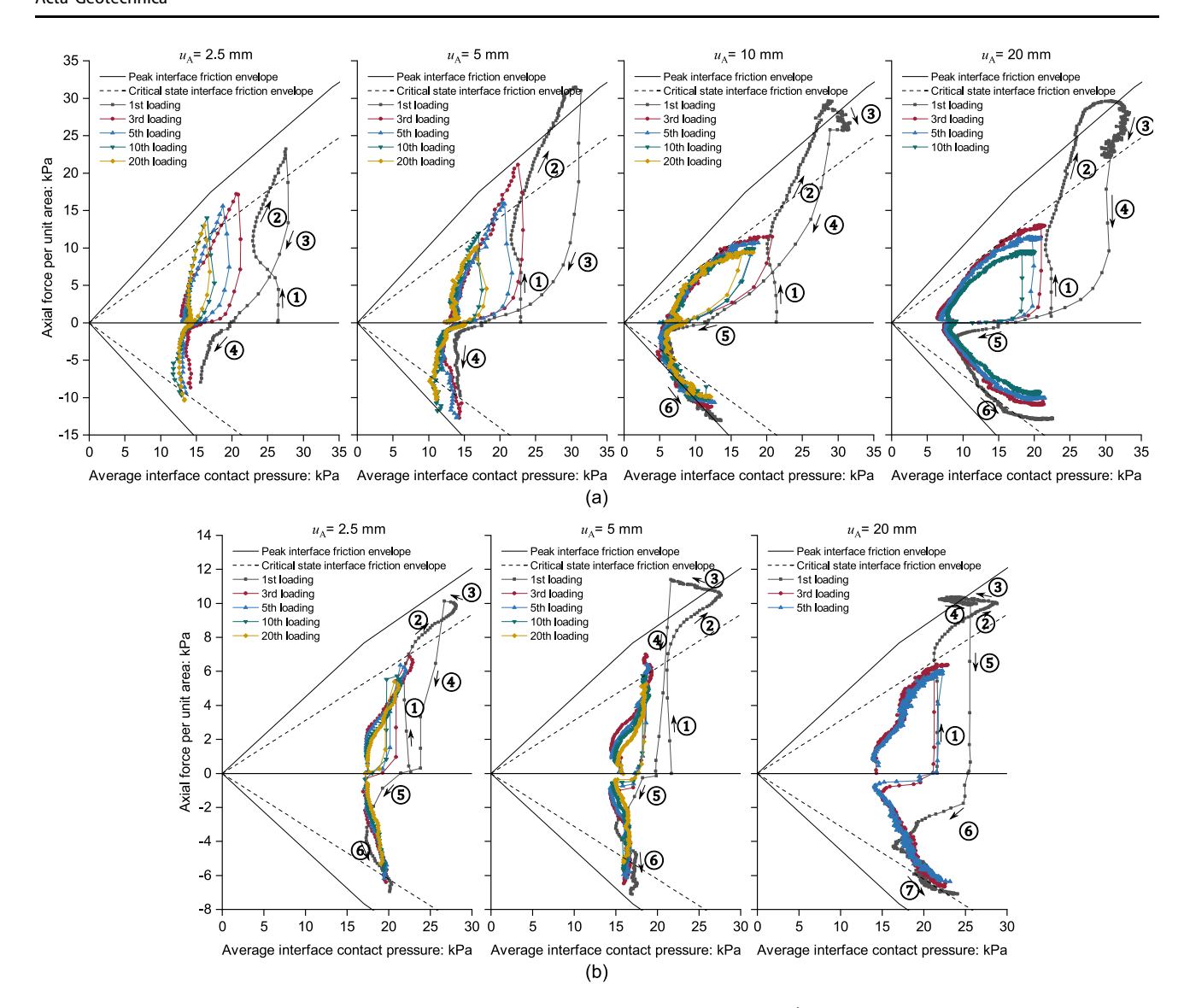


Fig. 12 Comparison between stress paths during cycling for different displacement amplitudes,  $\sigma_c' = 34$  kPa: (a) rough pipe and (b) smooth pipe

Fig. 13 illustrates the degradation of the maximum axial force for rough and smooth pipes under various displacement amplitudes over cycles, with a surcharge of 34 kPa. All values of the maximum axial force had consistently stabilized before the 20th cycle. Therefore, it was concluded that further degradation of the maximum axial force did not occur beyond 20 cycles, and, thus, the experiments were subsequently terminated. Except for the rough pipe at a 2.5 mm amplitude,  $T_{\rm u}$  converges to approximately 3.2 and 1.9 kN/m for rough and smooth pipes, respectively. The influence of amplitude is only obvious for the degradation rate.

Given the limited impacts of nominal pressure and cyclic amplitude on  $T_{\rm u}$ , as Fig. 5 and Fig. 13, the ultimate degradation factor can be seen as a function of pipe surface roughness and  $T_{\rm u}$  can be estimated using data from Fig. 5b

and the equation of  $T_1$  proposed by Guo and Zhou [15], as previously discussed.

### 3.6 Post-cyclic pullout behavior

Fig. 14 illustrates the post-cyclic pullout behavior in Series II with a nominal overburden pressure of 34 kPa. The results of the first and final loading with a displacement amplitude of 20 mm and a nominal overburden pressure of 34 kPa in Series I are also included for comparison. The former can be regarded as monotonic behavior without cycling, as the 20 mm displacement can mobilize a stable state (see Fig. 4). The latter can be regarded as post-cyclic behavior after cyclic loading with a 20 mm amplitude.

An obvious displacement-softening can be seen in the post-cyclic test on the rough pipe with a 2.5 mm cyclic



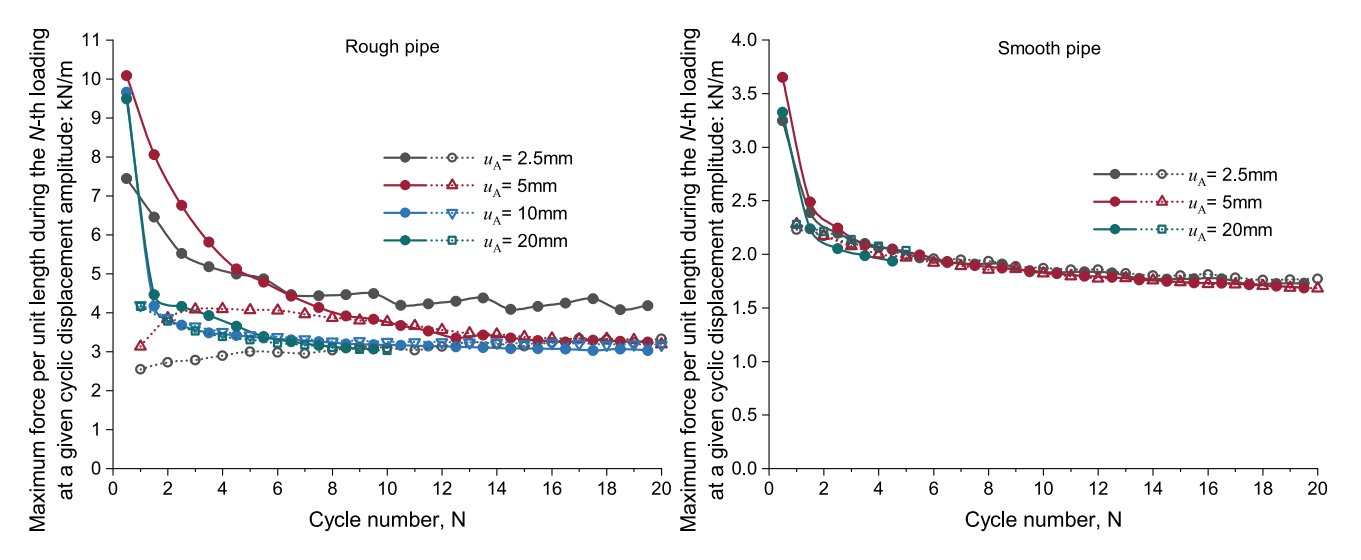


Fig. 13 Cyclic degradation of maximum axial force per unit length at a given cyclic displacement amplitude ( $\sigma_c' = 34 \text{ kPa}$ )

amplitude, while other tests on both rough and smooth pipes show displacement-hardening behavior. This finding is likely related to the fact that the stress path in the cyclic test with a 2.5 mm amplitude has not reached the failure envelope (see Fig. 12a). Hence, its stress path during the post-cyclic pullout process resembles the monotonic behavior, going downwards to the right after reaching the vicinity of the peak failure envelope. In contrast, only a tendency to move to the upper right can be seen in the stress paths of other tests.

To investigate the influence of cyclic loading on the post-cyclic pullout resistance, this study defines a post-cyclic change factor as the ratio  $T_{\rm p}/T_{\rm 1}$ , where  $T_{\rm p}$  is the axial resistance during the post-cyclic pullout, and  $T_{\rm 1}$  is essentially the monotonic resistance without cycling. As shown in Fig. 15, the change factor  $T_{\rm p}/T_{\rm 1}$  is greatly affected by the roughness and cyclic displacement amplitude. As expected, the difference between post-cyclic and monotonic resistances is consistently more significant when the pipe is rougher.

For the influence of cyclic displacement amplitude, two observations are included. On the one hand, taking the rough pipe as one example, the ratio is around 1.2 when the cyclic displacement is 2.5 mm, meaning that the post-cyclic pullout resistance is larger than the monotonic resistance by 20%. The cyclic loading-induced increase in pullout resistance is mainly attributed to larger soil-pipe interface contact pressure during pullout (see Fig. 14a). The observed effects of cyclic displacement amplitude on  $T_p/T_1$  may result from the shear band evolution at the soil-pipe interface. According to the cyclic interface shear tests by DeJong, Randolph et al. [44], the shear band at a smaller cyclic amplitude might not be as fully formed as that of monotonic loading. During the post-cyclic pullout, the

shear band might further develop, causing a further increase in soil-pipe interface contact pressure (see Fig. 11) and a pipe upward movement (see Fig. 14) due to constrained dilation. Moreover, the increase in average effective stress causes soil compression, tending to make soil denser and stronger. Furthermore, the higher values of  $T_{\rm p}$  after the cyclic loading may pose risks to the pipeline system. When there is any post-cyclic relative displacement between the pipe and soil, the stress imposed from soil to pipe may exceed the pipe strength if the pipeline design does not account for cyclic effects.

In contrast, the post-cyclic pullout resistance is smaller than the monotonic resistance because of a smaller soil-pipe interface contact pressure when the cyclic displacement is 5 mm or above. The ratio  $T_{\rm p}/T_{\rm 1}$  reduces significantly with an increase in roughness. The post-cyclic force–displacement curve of the rough pipe subjected to a 10 mm cyclic amplitude is very close to the final loading curve of the test at 20 mm amplitude. This proves a fully formed soil-pipe interface shear band during the cyclic stage of these tests.

### 4 Conclusions

A large-scale experimental system was utilized to explore the cyclic and post-cyclic axial behavior of steel pipes buried in dry and dense sand. This study presents and analyzes 12 tests with three levels of pipe surface roughness, three buried pressures, and four cyclic displacement amplitudes. The experimental findings led to several key conclusions:

At a given cyclic displacement of 20 mm, the maximum axial resistance during the first loading,  $T_1$ , exceeds the



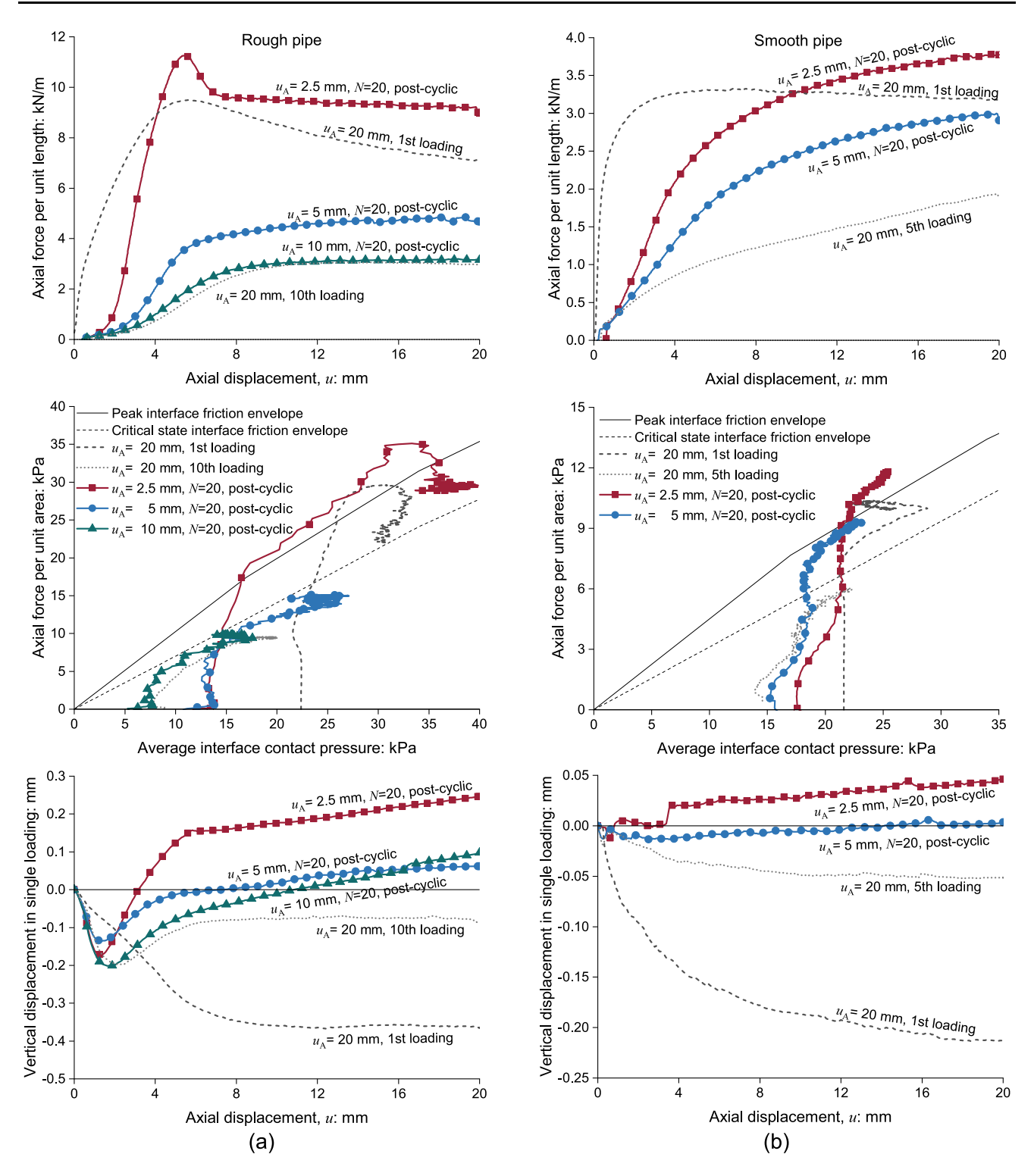
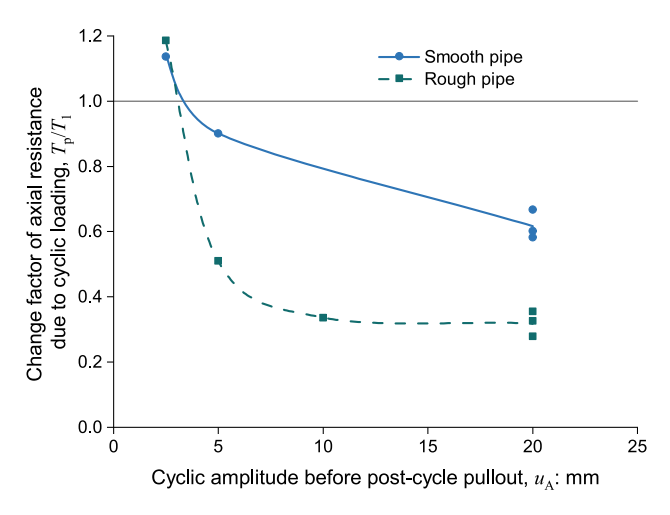


Fig. 14 Effects of cyclic displacement amplitude on post-cyclic pullout behavior ( $\sigma_c' = 34 \text{ kPa}$ ): (a) rough pipe and (b) smooth pipe

value predicted by the current design guidelines, using peak interface shear angle ( $\delta_{\rm peak}$ ). During subsequent cycles, the axial resistance degrades and stabilizes at an ultimate value,  $T_{\rm u}$ , which is typically lower than the predicted value, using the critical state interface shear angle

 $(\delta_{\rm cr})$ , with deviations up to 48%. Buried pressures and cyclic displacement amplitude exert a minimal influence on the ultimate degradation factor,  $T_{\rm u}/T_{\rm 1}$ . However, smaller cyclic displacement amplitudes slow the rate at which  $T_{\rm u}/T_{\rm 1}$  is reached. Pipe surface roughness has a decisive impact





**Fig. 15** Effects of pipe roughness and cyclic amplitude on the change factors of maximum axial resistance (i.e., the ratio of post-cyclic and monotonic pullout resistances) ( $\sigma_{\rm c}' = 34~{\rm kPa}$ )

on  $T_{\rm u}/T_1$ . The average values of  $T_{\rm u}/T_1$  for pipes with normalized roughness of 0.04, 0.21, and 1.01 are about 0.62, 0.39, and 0.32, respectively.

The evolution of soil arching plays an important role in cyclic ASPI based on the results of soil-pipe interface contact pressures, vertical earth pressures around the pipes, and pipe vertical displacement. Negative soil arching with constrained dilation increases interface contact pressure during the first loading, causing  $T_1$  to be larger than predicted. In subsequent cycles, soil compression due to the interface shear contraction/dilation behavior and the average effective stress variation leads to the pipe settlement. Ongoing settlement translates negative soil arching to positive soil arching on the upper part of the pipe, reducing interface contact pressure at the crown and shoulders. It causes the average interface contact pressure to be lower than predicted.

The post-cyclic pullout resistance is smaller than the monotonic resistance without cycling when the cyclic displacement is relatively large (above 5 mm in this study) due to interface contact pressure evolution, as illustrated above. In contrast, the post-cyclic pullout resistance is above the monotonic resistance when the cyclic displacement is smaller due to cyclic loading-induced soil densification. The difference between post-cyclic and monotonic resistances is consistently more significant when the pipe is rougher.

Based on the above findings, the following recommendations are proposed for the design of underground pipeline systems: (i) The increase in interface contact pressure caused by roughness-dependent constrained dilation should be considered when calculating the upper limit of axial resistance, as underestimating this effect may lead to unsafe pipeline design strength; (ii) Roughness-dependent

empirical values of  $T_{\rm u}/T_{\rm l}$  should be adopted to determine the lower limit of long-term axial resistance, which is crucial for estimating maximum pipe deformation; (iii) In scenarios where the pipe may experience relative ground movement after cycles, the effects of cyclic movement on post-cyclic pullout resistance should be incorporated based on test data.

A single pipe diameter and burial depth have been adopted in the current experimental study. When extrapolating the results of this study to pipes with different diameters and burial depths, the apparent interface friction coefficient (i.e.,  $T/(\pi D\sigma_c')$ ) presented in this study may serve as a useful reference. However, it should be noted that  $T/(\pi D\sigma_c')$  may vary slightly with pipe diameter and burial depth, owing to varying degrees of soil arching and constrained dilation effects. Meanwhile, the above tests were designed with reference to loading induced by temperature variations. The resulting frequency in the field is believed to be very low; therefore, the cycling frequency adopted in the tests ranged from 0.0005 to 0.004 Hz. Within this very low-frequency range, it is well recognized that frequency does not significantly affect soil behavior. However, if these results are to be applied to problems involving higher frequencies, such as seismic analysis, the influence of frequency should be considered, drawing on evidence from other studies in the literature.

**Acknowledgements** The authors would like to thank the Research Grants Council (RGC) of the HKSAR for providing financial support through grant N\_PolyU526/23 and AoE/E-603/18. This work was also supported by RISUD/PolyU under Grant 1-BBWS.

**Funding** Open access funding provided by The Hong Kong Polytechnic University. Research Grants Council, University Grants Committee, N\_PolyU526/23,Chao Zhou, AoE/E-603/18,Chao Zhou; Research Institute for Sustainable Urban Development, The Hong Kong Polytechnic University, 1-BBWS, Chao Zhou

Data availability Data will be made available on request.

#### **Declarations**

**Conflict of interest** The authors have no competing interests to declare that are relevant to the content of this article.

**Open Access** This article is licensed under a Creative Commons Attribution 4.0 International License, which permits use, sharing, adaptation, distribution and reproduction in any medium or format, as long as you give appropriate credit to the original author(s) and the source, provide a link to the Creative Commons licence, and indicate if changes were made. The images or other third party material in this article are included in the article's Creative Commons licence, unless indicated otherwise in a credit line to the material. If material is not included in the article's Creative Commons licence and your intended use is not permitted by statutory regulation or exceeds the permitted use, you will need to obtain permission directly from the copyright holder. To view a copy of this licence, visit <a href="http://creativecommons.org/licenses/by/4.0/">http://creativecommons.org/licenses/by/4.0/</a>.



### References

- ALA (2001) Guidelines for design of buried steel pipes. American lifelines alliance (ALA) in partnership with the federal emergency management agency (FEMA) and american society for civil engineers (ASCE). Reston. VA, US. https://www.americanlifelinesalliance.com/pdf/Update061305.pdf
- Saadawi H (2001) Upheaval buckling of gas injection pipelines onshore Abu Dhabi: a case study. In: Proceedings of SPE middle east oil show. Onepetro. Manama Bahrain. https://doi.org/10. 2118/68224-MS
- Zhang Q, Li Z, Huang H, Zhang H, Zheng H, Kuai H (2023) Stability of submarine bi-material pipeline-liner system with novel polyhedral composites subjected to thermal and mechanical loading fields. Mar Struct. https://doi.org/10.1016/j.marstruc. 2023.103424
- Jia H, Yang M, Dai L, Que Y, Wang D, Yu Z, Zhao Y, Hu W, Xu J, Tang J (2024) Centrifuge tests on the deformation law of pipelines crossing slopes with different water contents. Sci Rep. https://doi.org/10.1038/s41598-024-70372-z
- Ni PP, Moore ID, Take WA (2018) Distributed fibre optic sensing of strains on buried full-scale PVC pipelines crossing a normal fault. Geotech 68:1–17. https://doi.org/10.1680/jgeot.16.P.161
- Ni PP, Qin XG, Yi YL (2018) Use of tire-derived aggregate for seismic mitigation of buried pipelines under strike-slip faults. Soil Dyn Earthq Eng 115:495–506. https://doi.org/10.1016/j.soil dyn.2018.09.018
- Rizkalla M, Read RS (2019) Pipeline geohazards: planning, design, construction and operations, 2nd Edition. ASME Press, New York, NY, US
- Mortara G, Mangiola A, Ghionna VN (2007) Cyclic shear stress degradation and post-cyclic behaviour from sand-steel interface direct shear tests. Can Geotech J 44:739–752. https://doi.org/10. 1139/t07-019
- Rui SJ, Wang LZ, Guo Z, Zhou WJ, Li YJ (2020) Cyclic behavior of interface shear between carbonate sand and steel. Acta Geotech 16:189–209. https://doi.org/10.1007/s11440-020-01002-x
- Weidlich I, Achmus M (2008) Measurement of normal pressures and friction forces acting on buried pipes subjected to cyclic axial displacements in laboratory experiments. Geotech Test J 31:334–343. https://doi.org/10.1520/GTJ100804
- PRCI (2009) Guidelines for constructing natural gas and liquid hydrocarbon pipelines. Design, Materials, and Construction Committee of Pipeline Research Council International (PRCI). Chantilly, VA, US. https://rosap.ntl.bts.gov/view/dot/34640/dot\_ 34640\_DS1.pdf
- Vazouras P, Tsatsis A, Dakoulas P (2021) Thermal upheaval buckling of buried pipelines: experimental behavior and numerical modeling. J Pipeline Syst Eng Pract 12:04020057. https://doi. org/10.1061/(asce)ps.1949-1204.0000507
- ASCE (1984) Guidelines for the seismic design of oil and gas pipeline systems. Committee on Gas and Liquid Fuel Lifelines, American Society for Civil Engineering. New York, NY, US. https://cedb.asce.org/CEDBsearch/record.jsp?dockey=0042895
- Al-Khazaali M, Vanapalli SK (2019) Axial force–displacement behaviour of a buried pipeline in saturated and unsaturated sand. Geotech 69:986–1003. https://doi.org/10.1680/jgeot.17.P.116
- Guo C, Zhou C (2025) Axial behaviour of steel pipelines buried in sand: effects of surface roughness and hardness. Géotech 75:800–813. https://doi.org/10.1680/jgeot.24.00001
- Guo C, Zhou C (2025) Axial behaviour of underground steel pipeline buried in unsaturated soils. Tunn Undergr Sp Technol 164:106831. https://doi.org/10.1016/j.tust.2025.106831

- Guo C, Zhou C, Meguid MA (2025) Effect of surface roughness on axial soil-pipe interaction: a discrete element approach. Comput Geotech 187:107464. https://doi.org/10.1016/j.compgeo. 2025.107464
- Meidani M, Meguid MA, Chouinard LE (2017) Evaluation of soil-pipe interaction under relative axial ground movement.
   J Pipeline Syst Eng Pract 8:04017009. https://doi.org/10.1061/ (asce)ps.1949-1204.0000269
- Muntakim AH, Dhar AS (2021) Assessment of axial pullout force for buried medium-density polyethylene pipelines. J Pipeline Syst Eng Pract 12:04020074. https://doi.org/10.1061/(ASCE)PS.1949-1204.0000531
- Murugathasan P, Dhar AS, Hawlader BC (2021) An experimental and numerical investigation of pullout behavior of ductile iron water pipes buried in sand. Can J Civil Eng 48:134–143. https:// doi.org/10.1139/cjce-2019-0366
- Saberi M, Annan C-D, Sheil BB (2022) An efficient numerical approach for simulating soil-pipe interaction behaviour under cyclic loading. Comput Geotech 146:104666. https://doi.org/10. 1016/j.compgeo.2022.104666
- Sheil BB, Martin CM, Byrne BW, Plant M, Williams K, Coyne D (2018) Full-scale laboratory testing of a buried pipeline in sand subjected to cyclic axial displacements. Geotech 68:684–698. https://doi.org/10.1680/jgeot.16.P.275
- Wijewickreme D, Karimian H, Honegger D (2009) Response of buried steel pipelines subjected to relative axial soil movement. Can Geotech J 46:735–752. https://doi.org/10.1139/t09-019
- Bilgin Ö, Stewart HE (2009) Design guidelines for polyethylene pipe interface shear resistance. J Geotech Geoenviron Eng 135:809–818. https://doi.org/10.1061/(ASCE)GT.1943-5606. 0000030
- Di Donna A, Ferrari A, Laloui L (2016) Experimental investigations of the soil-concrete interface: physical mechanisms, cyclic mobilization, and behaviour at different temperatures. Can Geotech J 53:659–672. https://doi.org/10.1139/cgj-2015-0294
- Faizal M, Bouazza A, Haberfield C, McCartney JS (2018) Axial and radial thermal responses of a field-scale energy pile under monotonic and cyclic temperature changes. J Geotech Geoenviron Eng 144:04018072. https://doi.org/10.1061/(ASCE)GT.1943-5606.0001952
- Fakharian K, Evgin E (1997) Cyclic simple-shear behavior of sand-steel interfaces under constant normal stiffness condition.
   J Geotech Geoenviron Eng 123:1096–1105. https://doi.org/10. 1061/(ASCE)1090-0241(1997)123:12(1096)
- 28. Frost JD, Han J (1999) Behavior of interfaces between fiber-reinforced polymers and sands. J Geotech Geoenviron Eng 125:633–640. https://doi.org/10.1061/(ASCE)1090-0241(1999)125:8(633)
- Han F, Ganju E, Salgado R, Prezzi M (2018) Effects of interface roughness, particle geometry, and gradation on the sand–steel interface friction angle. J Geotech Geoenviron Eng 144:04018096. https://doi.org/10.1061/(asce)gt.1943-5606. 0001990
- Tian YH, Wu WC, Cassidy MJ, Randolph MF (2022) A complete analytical solution for axial pipeline walking considering seabed resistance as rigid plastic behaviour. Geotechnique 72:810–824. https://doi.org/10.1680/jgeot.20.P.135
- Zhou C, Tai P, Yin JH (2020) A bounding surface model for saturated and unsaturated soil-structure interfaces. Int J Numer Anal Methods Geomech 44:2412–2429. https://doi.org/10.1002/ nag.3123
- 32. DeJong JT, Westgate ZJ (2009) Role of initial state, material properties, and confinement condition on local and global soil-structure interface behavior. J Geotech Geoenviron Eng 135:1646–1660. https://doi.org/10.1061/(ASCE)1090-0241(2009)135:11(1646)



- Interlink (2023) FSR® integration guide & evaluation parts catalog with suggested electrical interfaces. Interlink Electronics. Camarillo, CA, US. http://www.tinyos.net.cn/datasheet/fsrguide. pdf. Accessed 14 December 2023
- Kootahi K, Leung AK (2022) Effect of soil particle size on the accuracy of tactile pressure sensors. J Geotech Geoenviron Eng 148:06022008. https://doi.org/10.1061/(asce)gt.1943-5606. 0002899
- Liu KY, Xu CS, Zhang XL (2021) Measurement performance evaluation of tactile pressure sensor with different particle sizes and sensor curvatures. Geotech Test J 44:1036–1054. https://doi. org/10.1520/GTJ20200028
- Guo C, Zhou C (2025) Novel single-point-type tactile pressure sensors for earth and soil-structure interface contact pressures measurement. Geotech Test J press. https://doi.org/10.1520/ GTJ20240066
- USBR (1996) Geotechnical training manual No. 7: Pipe bedding and backfill. United States department of the interior bureau of reclamation, technical service center geotechnical services. Denver, CO, US. https://www.usbr.gov/tsc/techreferences/mands/ mands-pdfs/pipebed.pdf
- 38. HKIUS (2011) Guide to utility management. Hong Kong Institute of Utility Specialists and Hong Kong Utility Research Centre. Hong Kong SAR. http://ibse.hk/MEBS6000/k.um.pdf
- WSD (2020) Guidelines for excavation near water mains. Water supplies department (WSD). Hong Kong SAR. https://www.wsd. gov.hk/en/publications-and-statistics/guidelines-reports-draw ings-specifications/guidelines-excavation/index.html
- 40. Kishida H, Uesugi M (1987) Tests of the interface between sand and steel in the simple shear apparatus. Geotech 37:45–52. https://doi.org/10.1680/geot.1987.37.1.45
- Paikowsky S, Player CM, Connors P (1995) A dual interface apparatus for testing unrestricted friction of soil along solid surfaces. Geotech Test J 18:168–193. https://doi.org/10.1520/ GTJ10320J
- 42. Mohitpour M, Golshan H, Murray A (2007) Pipeline design & construction: a practical approach, 3rd Edition. ASME Press, New York, NY, US
- Reza A, Dhar AS (2021) Axial pullout behavior of buried medium-hensity polyethylene gas distribution pipes. Int J Geomech 21:04021120. https://doi.org/10.1061/(ASCE)GM.1943-5622. 0002101
- 44. DeJong JT, Randolph MF, White DJ (2003) Interface load transfer degradation during cyclic loading: a microscale investigation. Soils Found 43:81–93. https://doi.org/10.3208/sandf.43. 4\_81

- 45. Pra-ai S, Boulon M (2016) Soil–structure cyclic direct shear tests: a new interpretation of the direct shear experiment and its application to a series of cyclic tests. Acta Geotech 12:107–127. https://doi.org/10.1007/s11440-016-0456-6
- Hubler JF, Athanasopoulos-Zekkos A, Zekkos D (2017) Monotonic, cyclic, and postcyclic simple shear response of three uniform gravels in constant volume conditions. J Geotech Geoenviron Eng 143:04017043. https://doi.org/10.1061/(ASCE)GT.1943-5606.0001723
- Zhou WH, Yin JH (2008) A simple mathematical model for soil nail and soil interaction analysis. Comput Geotech 35:479

  –488. https://doi.org/10.1016/j.compgeo.2007.07.001
- Grabowski A, Nitka M, Tejchman J (2020) 3D DEM simulations of monotonic interface behaviour between cohesionless sand and rigid wall of different roughness. Acta Geotech 16:1001–1026. https://doi.org/10.1007/s11440-020-01085-6
- Wang P, Yin ZY, Zhou WH, Chen WB (2022) Micro-mechanical analysis of soil–structure interface behavior under constant normal stiffness condition with DEM. Acta Geotech 17:2711–2733. https://doi.org/10.1007/s11440-021-01374-8
- Zhang G, Zhang JM (2006) Monotonic and cyclic tests of interface between structure and gravelly soil. Soils Found 46:505–518. https://doi.org/10.3208/sandf.46.505
- Bartlett SF, Lingwall BN, Vaslestad J (2015) Methods of protecting buried pipelines and culverts in transportation infrastructure using EPS geofoam. Geotext Geomembr 43:450–461. https://doi.org/10.1016/j.geotexmem.2015.04.019
- Costa YDJ, Zornberg JG (2020) Active and passive arching stresses outside a deep trapdoor. Acta Geotech 15:3211–3227. https://doi.org/10.1007/s11440-020-00969-x
- Meguid MA (2019) Earth pressure distribution on rigid pipes overlain by TDA inclusion. In: Badr M, Lotfy A (eds) Sustainable tunneling and underground use. GeoMEast 2018. Sustainable Civil Infrastructures. Springer, Cham. https://doi.org/10.1007/ 978-3-030-01884-9
- Ooi L, Carter J (1987) A constant normal stiffness direct shear device for static and cyclic loading. Geotech Test J 10:3–12. https://doi.org/10.1520/GTJ10132J
- Tejchman J, Wu W (1995) Experimental and numerical study of sand–steel interfaces. Int J Numer Anal Methods Geomech 19:513–536. https://doi.org/10.1002/nag.1610190803

**Publisher's Note** Springer Nature remains neutral with regard to jurisdictional claims in published maps and institutional affiliations.

